Nanoscale

COMMUNICATION

View Article Online
View Journal | View Issue

Cite this: *Nanoscale*, 2016, **8**, 1299

Received 7th November 2015,
Accepted 8th December 2015

DOI: 10.1039/c5nr07810e

www.rsc.org/nanoscale

Medium-sized $Au_{40}(SR)_{24}$ and $Au_{52}(SR)_{32}$ nanoclusters with distinct gold-kernel structures and spectroscopic features†

Wen Wu Xu,[a] Yadong Li,[a,b] Yi Gao*[a,c,d] and Xiao Cheng Zeng*[d,e]

We have analyzed the structures of two medium-sized thiolate-protected gold nanoparticles (RS-AuNPs) $Au_{40}(SR)_{24}$ and $Au_{52}(SR)_{32}$ and identified the distinct structural features in their Au kernels [*Sci. Adv.*, 2015, 1, e1500425]. We find that both Au kernels of the $Au_{40}(SR)_{24}$ and $Au_{52}(SR)_{32}$ nanoclusters can be classified as interpenetrating cuboctahedra. Simulated X-ray diffraction patterns of the RS-AuNPs with the cuboctahedral kernel are collected and then compared with the X-ray diffraction patterns of the RS-AuNPs of two other prevailing Au-kernels identified from previous experiments, namely the Ino-decahedral kernel and icosahedral kernel. The distinct X-ray diffraction patterns of RS-AuNPs with the three different types of Au-kernels can be utilized as signature features for future studies of structures of RS-AuNPs. Moreover, the simulated UV/Vis absorption spectra and Kohn–Sham orbital energy-level diagrams are obtained for the $Au_{40}(SR)_{24}$ and $Au_{52}(SR)_{32}$, on the basis of time-dependent density functional theory computation. The extrapolated optical band-edges of $Au_{40}(SR)_{24}$ and $Au_{52}(SR)_{32}$ are 1.1 eV and 1.25 eV, respectively. The feature peaks in the UV/Vis absorption spectra of the two clusters can be attributed to the d → sp electronic transition. Lastly, the catalytic activities of the $Au_{40}(SR)_{24}$ and $Au_{52}(SR)_{32}$ are examined using CO oxidation as a probe. Both medium-sized thiolate-protected gold clusters can serve as effective stand-alone nanocatalysts.

Introduction

Thiolate-protected gold nanoclusters (RS-AuNPs) have received considerable attention over the past decade owing to their unique structures and physicochemical properties compared with other types of gold nanoparticles,[1–7] and their potential applications in catalysis, nanotechnology, and biomedicine, among others.[8–11] To date, the total atomic structures of a number of RS-AuNPs, including $Au_{18}(SC_6H_{11})_{14}$,[12] $Au_{20}(TBBT)_{16}$ (TBBT = SPh-*p*-^{t}Bu),[13] $Au_{24\pm1}(SAdm)_{16}$,[14] $Au_{25}(PET)_{18}^{-1/0}$ (PET = phenylethylthiolate SCH_2CH_2Ph),[15–17] $Au_{28}(TBBT)_{20}$,[18] $Au_{30}S(S\text{-}t\text{-}Bu)_{18}$,[19] $Au_{36}(TBBT)_{24}$,[20] $Au_{38}(PET)_{24}$,[21] $Au_{102}(p\text{-}MBA)_{44}$ (*p*-MBA = *p*-mercaptobenzoic acid, $SC_7O_2H_5$),[22] $Au_{130}(p\text{-}MBT)_{50}$ (*p*-MBT = *para*-methylbenzenethiol),[23] $Au_{133}(TBBT)_{52}$,[24,25] *etc.* have been successfully resolved *via* X-ray crystallography. Among these clusters, $Au_{102}(p\text{-}MBA)_{44}$ and $Au_{25}(PET)_{18}^{-1/0}$ were the first two crystallized and characterized in 2007 and 2008, respectively. The total structure determination of $Au_{102}(p\text{-}MBA)_{44}$ and $Au_{25}(PET)_{18}^{-1/0}$ provides profound insights into many new characteristics such as gold–sulfur bonding, atomic packing structure in RS-AuNPs, staple motifs of ligands, as well as some generic rules of Au distribution among the Au-kernels and ligands. Until now, $Au_{133}(TBBT)_{52}$ is the largest ligand-covered gold cluster whose crystal structure has been obtained.

Although tremendous progress has been made in the structural determination of RS-AuNPs from small to large-size *via* X-ray crystallography, the crystal structures in the medium-size range from $Au_{38}(PET)_{24}$ to $Au_{102}(p\text{-}MBA)_{44}$ are largely unknown. The lack of crystal structures of medium-sized thiolate-protected gold clusters hinders the understanding of the structure–property relationship for many known stable clusters, such as $Au_{44}(TBBT)_{28}$,[26] $Au_{55}(PET)_{31}$,[27] $Au_{64}(SC_6H_{11})_{32}$,[28] $Au_{67}(PET)_{35}$,[29] $Au_{75}(SC_6H_{13})_{40}$,[30] $Au_{76}(4\text{-}MEBA)_{44}$ (4-MEBA = 4-(2-mercaptoethyl)benzoic acid),[31] and $Au_{99}(SPh)_{42}$,[32,33] all synthesized or isolated in the laboratory. Recently, Azubel *et al.* applied single-particle transmission electron microscopy (SP-TEM) to determine the positions of 68 Au atoms without a single crystal of $Au_{68}(3\text{-}MBA)_{32}$.[34] However, this SP-TEM

[a]*Division of Interfacial Water and Key Laboratory of Interfacial Physics and Technology, Shanghai Institute of Applied Physics, Chinese Academy of Sciences, Shanghai 201800, China. E-mail: gaoyi@sinap.ac.cn*
[b]*University of Chinese Academy of Sciences, Beijing 100049, China*
[c]*Shanghai Science Research Center, Chinese Academy of Sciences, Shanghai 201204, China*
[d]*Department of Chemistry, University of Nebraska-Lincoln, Lincoln, NE 68588, USA. E-mail: xzeng1@unl.edu*
[e]*Collaborative Innovation Center of Chemistry for Energy Materials, University of Science and Technology of China, Hefei, Anhui 230026, China*
†Electronic supplementary information (ESI) available. See DOI: 10.1039/c5nr07810e

measurement still requires theoretical input on the protection ligands to achieve the total structure of the cluster.

Very recently, two medium-sized clusters, $Au_{40}(o\text{-MBT})_{24}$ and $Au_{52}(TBBT)_{32}$, have been successfully crystallized by Zeng *et al.*[35] It was found that both nanoclusters are composed of 4-atom tetrahedral units which can coil up into a Kekulé-like ring in the $Au_{40}(o\text{-MBT})_{24}$ (*o*-MBT = *ortho*-methylbenzenethiol) cluster or a DNA-like double helix in $Au_{52}(TBBT)_{32}$. In particular, the $Au_{52}(TBBT)_{32}$ cluster is a new species to the RS-AuNP family, while the $Au_{40}(o\text{-MBT})_{24}$ cluster is akin to the known phenylethylthiolate-capped $Au_{40}(PET)_{24}$ cluster which is an intermediate in the synthesis of the $Au_{38}(PET)_{24}$ cluster.[36,37] However, the marked differences in the absorption spectrum indicate that $Au_{40}(o\text{-MBT})_{24}$ and $Au_{40}(PET)_{24}$ have different structures.[38] The Kekulé-like ring in $Au_{40}(o\text{-MBT})_{24}$ is completely different from the Au_{26} bi-icosahedral core in the $Au_{40}(PET)_{24}$ originally proposed by Malola *et al.*[39] The experimental work by Zeng *et al.* sheds new light on the total structures of RS-AuNPs within the range of $Au_{38}(PET)_{24}$ and $Au_{102}(p\text{-MBA})_{44}$.[35]

In this communication, we perform an in-depth kernel structure analysis of $Au_{40}(o\text{-MBT})_{24}$ and $Au_{52}(TBBT)_{32}$. We classify all known RS-AuNPs into three groups: (1) cuboctahedra, (2) Ino-decahedra, and (3) icosahedra. The calculated powder X-ray diffraction (XRD) results reveal different characteristic peaks for the Au-kernel structures in these groups, which can be useful in identifying the structures of gold nanoparticles even when the crystal structure is lacking. In addition, the computed optical absorption spectra of $Au_{40}(o\text{-MBT})_{24}$ and $Au_{52}(TBBT)_{32}$ are found to be consistent with experimental measurements. Lastly, the catalytic properties of both clusters are examined by using CO oxidation as a probe.

Computational methods

The theoretical powder X-ray diffraction (XRD) curve is calculated using the Debye formula:

$$I(s) = \sum_i \sum_{j \neq i} \frac{\cos\theta}{(1 + \alpha\cos(2\theta))} \exp\left(-\frac{Bs^2}{2}\right) f_i f_j \frac{\sin(2\pi d_{ij})}{2\pi d_{ij}},$$

where s is the diffraction vector length and θ is the scattering angle, satisfying $s = 2\sin\theta/\lambda$. λ and α are determined by the experimental setup and are set to be 0.1051967 nm and 1.01, respectively. B is the damping factor, which reflects thermal vibrations, and is set to be 0.03 nm^2. The corresponding atomic numbers are used for the scattering factors f_i. d_{ij} is the distance between atoms i and j. The atomic distance d_{ij} is taken from the optimized structure of clusters based on the density functional theory (DFT) code $DMol^3$ (version 7.0).[40,41] The generalized gradient approximation with the Perdew–Burke–Ernzerhof (PBE)[42] functional and the double numeric polarized (DNP) basis set coupled with semi-core pseudopotential are employed. Self-consistent calculations are done with a convergence criterion of 10^{-5} hartree for the total energy. The linear and quadratic synchronous transit (LST/QST) method is used to locate the transition state of CO oxidation on the $Au_{40}(o\text{-MBT})_{24}$ and $Au_{52}(TBBT)_{32}$.[43–48] In all calculations, the *o*-MBT in $Au_{40}(o\text{-MBT})_{24}$, TBBT in $Au_{52}(TBBT)_{32}$, and the ligands of other RS-AuNPs are simplified by methyl groups to lower computation cost.

Results and discussion

To understand the structure formation of $Au_{40}(SR)_{24}$ and $Au_{52}(SR)_{32}$, their kernel structures are analyzed first. The formation of the Au_{34} kernel of $Au_{40}(SR)_{24}$ can be divided into two steps, with the Au_{13} cuboctahedra as building blocks, as shown in Fig. 1. In step 1, the two Au_{13} cuboctahedra interpenetrate each other to form a Au_{20} structure by sharing six Au atoms. This rod-like Au_{20} geometry has been found as a kernel in the structures of $Au_{28}(SR)_{20}$ and $Au_{30}S(SR)_{18}$.[18,19] Next, one of the Au_{13} cuboctahedra in the Au_{20} interpenetrates with the other two Au_{13} cuboctahedra in the same way as in step 1 to form the kernel of Au_{34} with a fcc-like structure. Likewise, as shown in Fig. 2, the formation of the Au_{44} kernel of $Au_{52}(SR)_{32}$ can be divided into three steps in the same way as Au_{40} in $Au_{40}(SR)_{24}$. In step 1 three Au_{20} geometries interpenetrate each other to form an Au_{25} structure. Next, the Au_{25} structure interpenetrates with another Au_{13} cuboctahedra to form a Au_{28} geometry, a kernel found in the structure of $Au_{36}(SR)_{24}$.[17] In step 3, the Au_{44} kernel with fcc-like symmetry can be formed through two interpenetrating Au_{28} geometries. The above structure analysis on the kernels of $Au_{40}(SR)_{24}$ and $Au_{52}(SR)_{32}$, as well as $Au_{28}(SR)_{20}$, $Au_{30}S(SR)_{18}$, and $Au_{36}(SR)_{24}$ (ESI Fig. S1†), shows that the Au kernels of all these clusters with

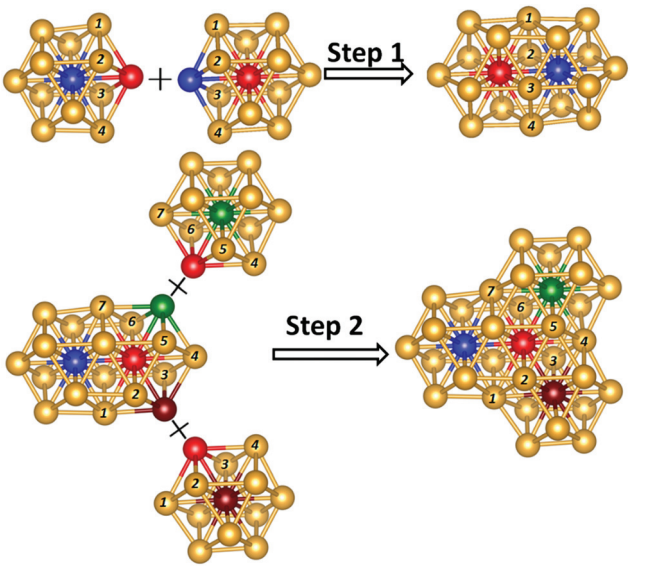

Fig. 1 The formation of Au_{34} kernel in $Au_{40}(SR)_{24}$. The Au atoms marked with the same number and color can be fused together.

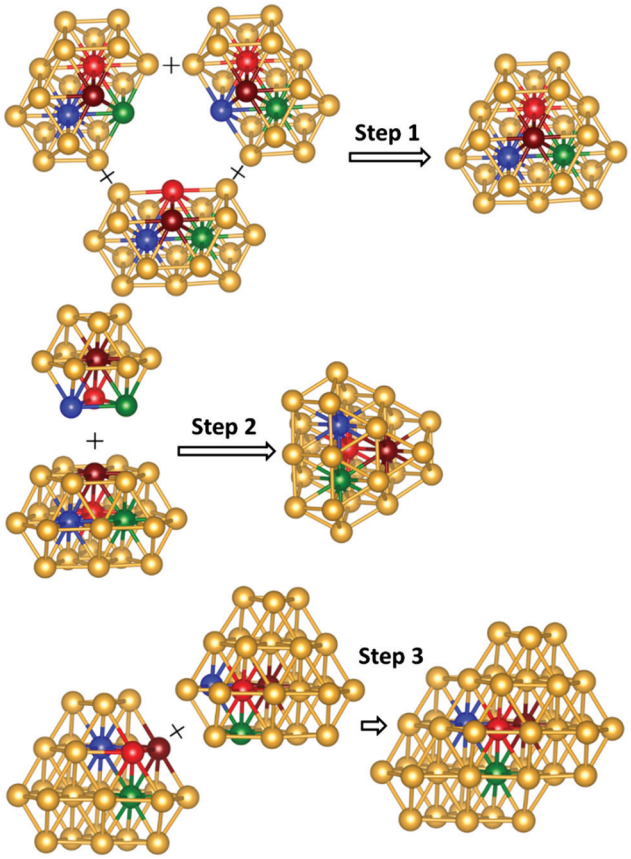

Fig. 2 The formation of Au_{44} kernel in $Au_{52}(SR)_{32}$. The Au atoms marked with the same color can be fused together.

fcc-like symmetry are comprised of several interpenetrating cuboctahedra.

Besides $Au_{28}(SR)_{20}$, $Au_{30}S(SR)_{18}$, $Au_{36}(SR)_{24}$, $Au_{40}(SR)_{24}$, and $Au_{52}(SR)_{32}$, structure analysis for the kernels of other RS-AuNPs such as $Au_{25}(SR)_{18}$, $Au_{38}(SR)_{24}$, $Au_{102}(SR)_{44}$, $Au_{130}(SR)_{50}$, and $Au_{133}(SR)_{52}$ are presented in ESI Fig. S2 and S3.† Interestingly, according to different types of kernel structures, those crystallized RS-AuNPs larger than $Au_{25}(SR)_{18}$ can be classified into three categories, as shown in Fig. 3: the first category includes $Au_{28}(SR)_{20}$, $Au_{30}S(SR)_{18}$, $Au_{36}(SR)_{24}$, $Au_{40}(SR)_{24}$, and $Au_{52}(SR)_{32}$, whose Au kernels possess fcc-like symmetry, are comprised of several interpenetrating cuboctahedra. The $Au_{102}(SR)_{44}$ and $Au_{130}(SR)_{50}$ nanoclusters in which the Au kernels possess Ino-decahedral (D_{5h}) symmetry can be grouped into the second category. The last category includes the remaining RS-AuNPs such as $Au_{25}(SR)_{18}$ and $Au_{133}(SR)_{52}$ with icosahedral Au kernels, and $Au_{38}(SR)_{24}$ with a fused biicosahedral kernel.

Simulated powder X-ray diffraction (XRD) curves of these crystallized RS-AuNPs exhibit different characteristic peaks for nanoclusters with different Au kernel structures. First, we confirm the reliability of the theoretical formula for computing the XRD curves by comparing the simulated XRD curves and the measured XRD curves of $Au_{25}(SR)_{18}$ and $Au_{38}(SR)_{24}$, as

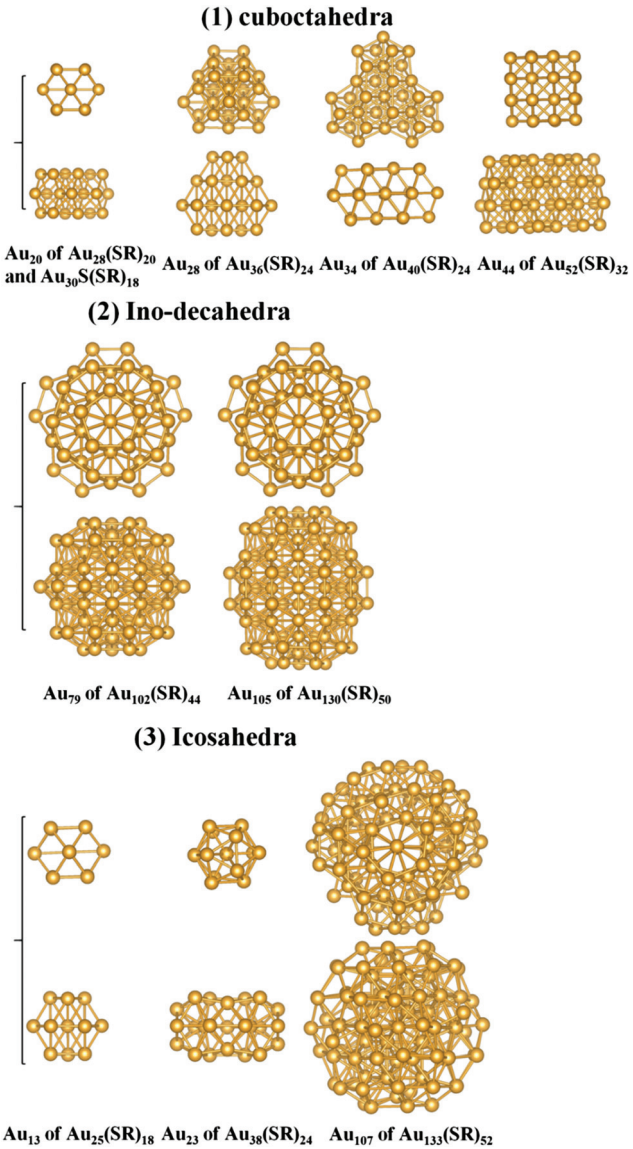

Fig. 3 Two orthogonal views of the Au kernels of the crystallized RS-AuNPs larger than $Au_{25}(SR)_{18}$, all classified into three categories: (1) cuboctahedra, (2) Ino-decahedra, and (3) icosahedra.

shown in ESI Fig. S4.† Next, the XRD spectra of the RS-AuNPs in all three categories are presented in Fig. 4. From Fig. 4(a), one can see that the $Au_{28}(SR)_{20}$, $Au_{30}S(SR)_{18}$, $Au_{36}(SR)_{24}$, $Au_{40}(SR)_{24}$, and $Au_{52}(SR)_{32}$ nanoclusters exhibit similar diffraction patterns, where a main peak is located at about 4.0 nm^{-1}, and the two weaker peaks are located at 6.5 nm^{-1} and 7.5 nm^{-1}, respectively. In the second category (Fig. 4(b)), the consistent XRD curves of $Au_{102}(SR)_{44}$ and $Au_{130}(SR)_{50}$ nanoclusters, where only one less pronounced peak is located at 7.7 nm^{-1}, are significantly different from those in the first category. For the last category, as shown in Fig. 4(c), the diffraction pattern of the $Au_{133}(SR)_{52}$ nanocluster, where four weaker peaks are located in the range 5–9 nm^{-1}, differ from those of $Au_{25}(SR)_{18}$ and $Au_{38}(SR)_{24}$. The multi-peak diffraction

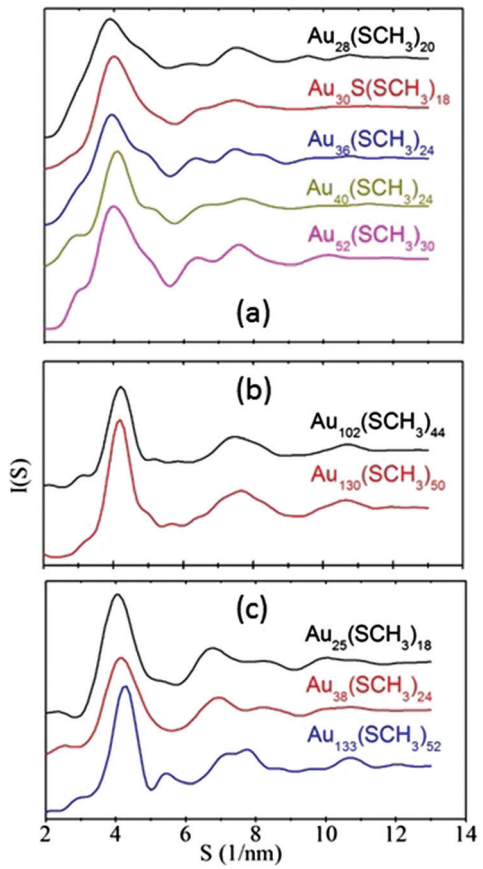

Fig. 4 Theoretical powder X-ray diffraction (XRD) curves of the crystallized RS-AuNPs.

pattern can be attributed to the multi-shell structure of the $Au_{133}(SR)_{52}$ nanocluster. The analysis above shows that the diffraction pattern is closely related to the structure of the Au kernel in RS-AuNP, which can offer clues to theoretical prediction of the structure of RS-AuNP even when the single crystal is lacking.

Fig. 5 presents the simulated UV/Vis optical absorption spectra of $Au_{40}(SR)_{24}$ and $Au_{52}(SR)_{32}$ based on the time-dependent DFT (TD-DFT) computation. In addition, the atomic orbital (AO) component of Kohn–Sham molecular orbitals is displayed. As shown in Fig. 5(a), the extrapolated optical band-edge of $Au_{40}(SR)_{24}$ is 1.1 eV, consistent with the measured optical gap.[39] The extrapolated optical band-edge of $Au_{52}(SR)_{32}$ is 1.25 eV (Fig. 5(c)). The population analysis of Kohn–Sham (KS) molecular orbitals, as shown in Fig. 5(b) and (d), demonstrates that the occupied frontier molecular orbitals are mainly contributed from the Au(5d), denoted as the d band, while the Au(6sp) atomic orbitals show dominant contributions to the unoccupied orbitals (sp band). The feature absorption peaks can therefore be assigned to the d → sp interband transition.

Finally, the catalytic properties of $Au_{40}(SR)_{24}$ and $Au_{52}(SR)_{32}$ are examined by using CO oxidation as a probe. To this end, a few surface staple motifs on the clusters are removed to allow for the catalytic reaction.[49,50] The computed catalytic reaction pathway for CO oxidation on the $Au_{40}(SR)_{24}$ cluster is shown in Fig. 6(a). CO and O_2 are coadsorbed initially with a binding energy of −1.76 eV. Then the O_2 molecule moves toward the adsorbed CO molecule to form a bridge-like metastable intermediate state characterized by the O–C–O–O species with the

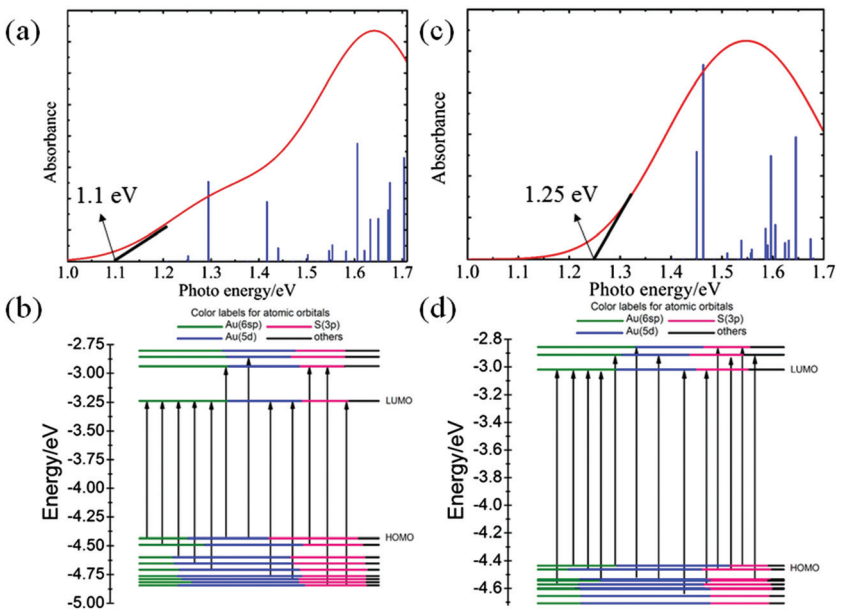

Fig. 5 Simulated UV/Vis absorption spectra and Kohn–Sham orbital energy level diagrams of $Au_{40}(SR)_{24}$ (a and b) and $Au_{52}(SR)_{32}$ (c and d). The energies are in eV. Each Kohn–Sham orbital is drawn to show the relative contributions (line length with color labels) of the atomic orbitals of Au(6sp) olive, Au(5d) blue, S(3p) magenta, and other orbital contributions from C and H atoms are in black.

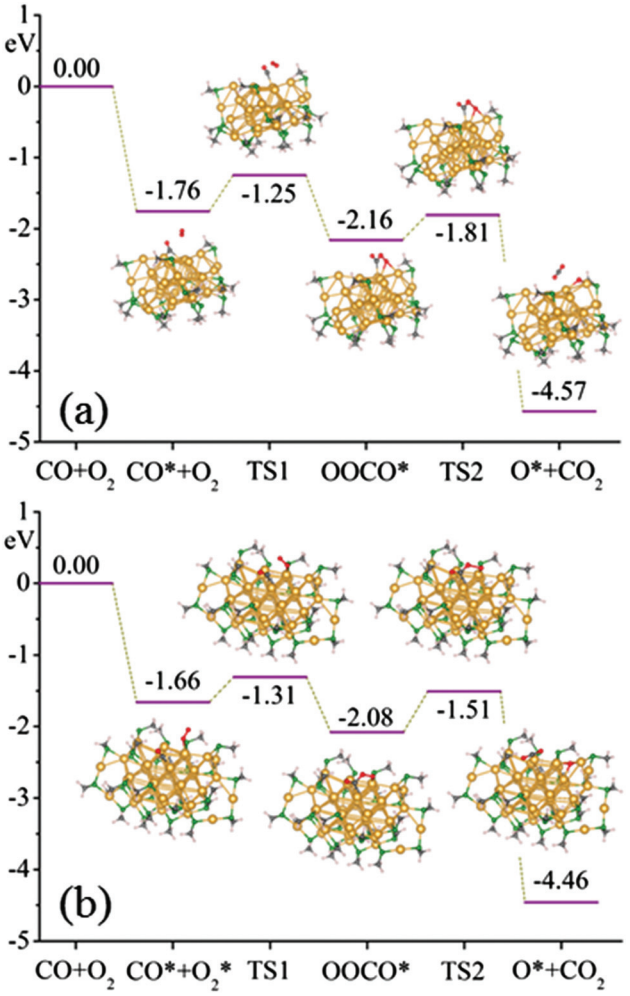

Fig. 6 Computed reaction pathway for the CO oxidation on $Au_{40}(SR)_{24}$ (a) and $Au_{52}(SR)_{32}$ (b) clusters. Here, the symbol * denotes adsorption of the corresponding molecules on Au atoms. Au, S, C, O, and H atoms are in gold, olive, dark gray, red, and white, respectively.

O–O bond length being 1.45 Å, and the CO oxidation requires overcoming a reaction barrier of 0.51 eV (TS1). The O–O bond length is further elongated to 1.81 Å, while CO fully grasps an O atom of O_2 to form a CO_2 molecule. The CO_2 can eventually desorb by overcoming a relatively low-energy barrier of 0.35 eV (TS2), leaving the other O atom adsorbed on the gold cluster.

For CO oxidation on the $Au_{52}(SR)_{32}$ cluster, as shown in Fig. 6(b), the CO and O_2 molecules can be favorably co-adsorbed on two neighboring low-coordinated Au atoms, with the coadsorption energy of CO and O_2 being about −1.66 eV. The reaction pathway is similar to that for the $Au_{40}(SR)_{24}$, in which the two molecular species require to overcome reaction barriers of 0.35 eV (TS1) and 0.57 eV (TS2), respectively, to arrive at the final product state. Both reaction barriers are comparable to those of typical nanogold catalysts,[51–53] indicating that the $Au_{40}(SR)_{24}$ and $Au_{52}(SR)_{32}$ clusters can be a stand-alone nanoscale catalyst for CO oxidation.

Conclusions

We have performed a systematic structure analysis of two medium-sized $Au_{40}(SR)_{24}$ and $Au_{52}(SR)_{32}$ nanoclusters. We find that the kernel structures of both nanoclusters can be viewed as several interpenetrating cuboctahedra. Based on this observation, we suggest classification of the crystallized RS-AuNPs into three groups according to their kernel structures. In the first group, Au kernels of RS-AuNPs such as $Au_{28}(SR)_{20}$, $Au_{30}S(SR)_{18}$, $Au_{36}(SR)_{24}$, $Au_{40}(SR)_{24}$, and $Au_{52}(SR)_{32}$ exhibit fcc-like symmetry, comprising several interpenetrating cuboctahedra. In the second group, Au kernels of RS-AuNPs such as $Au_{102}(SR)_{44}$ and $Au_{130}(SR)_{50}$ possess Ino-decahedral (D_{5h}) symmetry. The third group includes $Au_{25}(SR)_{18}$, $Au_{133}(SR)_{52}$ with icosahedral Au kernels, or $Au_{38}(SR)_{24}$ with a fused icosahedral Au kernel. Clusters in each group give rise to distinct diffraction patterns, thereby providing important clues for the theoretical prediction of the structure of RS-AuNPs as long as the XRD data are known. We have also computed the UV/Vis absorption spectra and Kohn–Sham orbital energy level diagrams for $Au_{40}(SR)_{24}$ and $Au_{52}(SR)_{32}$. Our calculation indicates that the first absorption peak can be assigned to the d → sp interband transition. Examination of the catalytic properties of $Au_{40}(SR)_{24}$ and $Au_{52}(SR)_{32}$ suggests that both clusters can be stand-alone nanoscale catalysts for CO oxidation.

Acknowledgements

W. W. X. is supported by the China Postdoctoral Science Foundation Project (Y419022011, Y519031011), and the National Natural Science Foundation of China (11504396). Y. G. is supported by the startup funding from the Shanghai Institute of Applied Physics, the Chinese Academy of Sciences (Y290011011), the National Natural Science Foundation of China (21273268, 11574340), the "Hundred People Project" from the Chinese Academy of Sciences, the "Pu-jiang Rencai Project" from the Science and Technology Commission of Shanghai Municipality (13PJ1410400), and the CAS-Shanghai Science Research Center (CAS-SSRC-YJ-2015-01). The computational resources utilized in this research were provided by the Shanghai Supercomputer Center, the National Supercomputing Center in Tianjin and the Supercomputing Center of the Chinese Academy of Sciences in Beijing. X. C. Z. is supported by a grant from the Nebraska Center for Energy Sciences Research and a USTC fund for the 1000-Talents B program (summer research).

References

1 M. M. Alvarez, J. T. Khoury, T. G. Schaaff, M. N. Shafigullin, I. Vezmar and R. L. Whetten, *J. Phys. Chem. B*, 1997, **101**, 3706–3712.
2 Y. Negishi, K. Nobusada and T. Tsukuda, *J. Am. Chem. Soc.*, 2005, **127**, 5261–5270.

3 S. Chen, R. S. Ingram, M. J. Hostetler, J. J. Pietron, R. W. Murray, T. G. Schaaff, J. T. Khoury, M. M. Alvarez and R. L. Whetten, *Science*, 1998, **280**, 2098–2101.
4 A. S. K. Hashmi and G. J. Hutchings, *Angew. Chem., Int. Ed.*, 2006, **45**, 7896–7936.
5 H. Häkkinen, *Nat. Chem.*, 2012, **4**, 443–455.
6 Y. Pei and X. C. Zeng, *Nanoscale*, 2012, **4**, 4054–4072.
7 H. Qian, M. Zhu, Z. Wu and R. Jin, *Acc. Chem. Res.*, 2012, **45**, 1470–1479.
8 R. W. Murray, *Chem. Rev.*, 2008, **108**, 2688–2720.
9 R. Jin, *Nanoscale*, 2010, **2**, 343–362.
10 R. Jin, *Nanoscale*, 2015, **7**, 1549–1565.
11 P. Maity, S. Xie, M. Yamauchi and T. Tsukuda, *Nanoscale*, 2012, **4**, 4027–4037.
12 A. Das, C. Liu, H. Y. Byun, K. Nobusada, S. Zhao, N. Rosi and R. Jin, *Angew. Chem., Int. Ed.*, 2015, **54**, 3140–3144.
13 C. Zeng, C. Liu, Y. Chen, N. L. Rosi and R. Jin, *J. Am. Chem. Soc.*, 2014, **136**, 11922–11925.
14 D. Crasto, G. Barcaro, M. Stener, L. Sementa, A. Fortunelli and A. Dass, *J. Am. Chem. Soc.*, 2014, **136**, 14933–14940.
15 M. Zhu, C. M. Aikens, F. J. Hollander, G. C. Schatz and R. Jin, *J. Am. Chem. Soc.*, 2008, **130**, 5883–5885.
16 J. Akola, M. Walter, R. L. Whetten, H. Häkkinen and H. Grönbeck, *J. Am. Chem. Soc.*, 2008, **130**, 3756–3757.
17 M. W. Heaven, A. Dass, P. S. White, K. M. Holt and R. W. Murray, *J. Am. Chem. Soc.*, 2008, **130**, 3754–3755.
18 C. Zeng, T. Li, A. Das, N. L. Rosi and R. Jin, *J. Am. Chem. Soc.*, 2013, **135**, 10011–10013.
19 D. Crasto, S. Malola, G. Brosofsky, A. Dass and H. Häkkinen, *J. Am. Chem. Soc.*, 2014, **136**, 5000–5005.
20 C. Zeng, H. Qian, T. Li, G. Li, N. L. Rosi, B. Yoon, R. N. Barnett, R. L. Whetten, U. Landman and R. Jin, *Angew. Chem., Int. Ed.*, 2012, **51**, 13114–13118.
21 H. Qian, W. T. Eckenhoff, Y. Zhu, T. Pintauer and R. Jin, *J. Am. Chem. Soc.*, 2010, **132**, 8280–8281.
22 P. D. Jadzinsky, G. Calero, C. J. Ackerson, D. A. Bushnell and R. D. Kornberg, *Science*, 2007, **318**, 430–433.
23 Y. Chen, C. Zeng, C. Liu, K. Kirschbaum, C. Gayathri, R. R. Gil, N. L. Rosi and R. Jin, *J. Am. Chem. Soc.*, 2015, **137**, 10076–10079.
24 A. Dass, S. Theivendran, P. R. Nimmala, C. Kumara, V. R. Jupally, A. Fortunelli, L. Sementa, G. Barcaro, X. Zuo and B. C. Noll, *J. Am. Chem. Soc.*, 2015, **137**, 4610–4613.
25 C. Zeng, Y. Chen, K. Kirschbaum, K. Appavoo, M. Y. Sfeir and R. Jin, *Sci. Adv.*, 2015, **1**, e1500045.
26 C. Zeng, Y. Chen, G. Li and R. Jin, *Chem. Commun.*, 2014, **50**, 55–57.
27 H. Qian and R. Jin, *Chem. Commun.*, 2011, **47**, 11462–11464.
28 C. Zeng, Y. Chen, G. Li and R. Jin, *Chem. Mater.*, 2014, **26**, 2635–2641.
29 P. R. Nimmala, B. Yoon, R. L. Whetten, U. Landman and A. Dass, *J. Phys. Chem. A*, 2013, **117**, 504–517.
30 R. Balasubramanian, R. Guo, A. J. Mills and R. W. Murray, *J. Am. Chem. Soc.*, 2005, **127**, 8126.
31 S. Takano, S. Yamazoe, K. Koyasu and T. Tsukuda, *J. Am. Chem. Soc.*, 2015, **137**, 7027–7030.
32 G. Li, C. Zeng and R. Jin, *J. Am. Chem. Soc.*, 2014, **136**, 3673–3679.
33 P. R. Nimmala and A. Dass, *J. Am. Chem. Soc.*, 2014, **136**, 17016–17023.
34 M. Azubel, J. Koivisto, S. Malola, D. Bushnell, G. L. Hura, A. L. Koh, H. Tsunoyama, T. Tsukuda, M. Pettersson, H. Häkkinen and R. D. Kornberg, *Science*, 2014, **345**, 909–912.
35 C. Zeng, Y. Chen, C. Liu, K. Nobusada, N. Rosi and R. Jin, *Sci. Adv.*, 2015, **1**, e1500425.
36 H. Qian, Y. Zhu and R. Jin, *J. Am. Chem. Soc.*, 2010, **132**, 4583–4585.
37 S. Knoppe, J. Boudon, I. Dolamic, A. Dass and T. Bürgi, *Anal. Chem.*, 2011, **83**, 5056–5061.
38 Y. Chen, C. Zeng, D. R. Kauffman and R. Jin, *Nano Lett.*, 2015, **15**, 3603–3609.
39 S. Malola, L. Lehtovaara, S. Knoppe, K. J. Hu, R. E. Palmer, T. Burgi and H. Häkkinen, *J. Am. Chem. Soc.*, 2012, **134**, 19560–19563.
40 B. Delley, *J. Chem. Phys.*, 1990, **92**, 508–517.
41 B. Delley, *J. Chem. Phys.*, 2003, **113**, 7756–7764. DMoL3 is available from Accelrys.
42 J. P. Perdew, K. Burke and M. Ernzerhof, *Phys. Rev. Lett.*, 1996, **77**, 3865–3868.
43 W. W. Xu, Y. Gao and X. C. Zeng, *Sci. Adv.*, 2015, **1**, e1400211.
44 W. W. Xu and Y. Gao, *J. Phys. Chem. C*, 2015, **119**, 14224–14229.
45 Y. Pei, Y. Gao, N. Shao and X. C. Zeng, *J. Am. Chem. Soc.*, 2009, **131**, 13619–13621.
46 Y. Pei, R. Pal, C. Liu, Y. Gao, Z. Zhang and X. C. Zeng, *J. Am. Chem. Soc.*, 2012, **134**, 3015–3024.
47 Y. Pei, Y. Gao and X. C. Zeng, *J. Am. Chem. Soc.*, 2008, **130**, 7830–7832.
48 Y. Pei, S. S. Lin, J. Su and C. Liu, *J. Am. Chem. Soc.*, 2013, **135**, 19060–19063.
49 O. Lopez-Acevedo, K. A. Kacprzak, J. Akola and H. Häkkinen, *Nat. Chem.*, 2010, **2**, 329–334.
50 Z. Wu, D. Jiang, A. K. P. Mann, D. R. Mullins, Z. Qiao, L. F. Allard, C. Zeng, R. Jin and S. H. Overbury, *J. Am. Chem. Soc.*, 2014, **136**, 6111–6122.
51 H. Li, L. Li, A. Pedersen, Y. Gao, N. Khetrapal, H. Jónsson and X. C. Zeng, *Nano Lett.*, 2015, **15**, 682–688.
52 Y. Gao, N. Shao, Y. Pei, Z. Chen and X. C. Zeng, *ACS Nano*, 2011, **5**, 7818–7829.
53 C. Liu, Y. Tan, S. Lin, H. Li, X. Wu, L. Li, Y. Pei and X. C. Zeng, *J. Am. Chem. Soc.*, 2013, **135**, 2583–2595.

